Aurélie Ortolan[1]
Aerodynamic Department,
SAFRAN Ventilation Systems,
Blagnac 31700, France;
Department of Aerodynamics,
Energetics and Propulsion,
Université de Toulouse ISAE-SUPAERO,
Toulouse 31400, France
e-mail: aurelie.ortolan@isae.fr

Suk-Kee Courty-Audren
Department of Aerodynamics,
Energetics and Propulsion,
Université de Toulouse ISAE-SUPAERO,
Toulouse 31400, France

Massyl Lagha
Department of Aerodynamics,
Energetics and Propulsion,
Université de Toulouse ISAE-SUPAERO,
Toulouse 31400, France

Nicolas Binder
Department of Aerodynamics,
Energetics and Propulsion,
Université de Toulouse ISAE-SUPAERO,
Toulouse 31400, France

Xavier Carbonneau
Department of Aerodynamics,
Energetics and Propulsion,
Université de Toulouse ISAE-SUPAERO,
Toulouse 31400, France

Florent Challas
Aerodynamic Department,
SAFRAN Ventilation Systems,
Blagnac 31700, France

Generic Properties of Flows in Low-Speed Axial Fans Operating at Load-Controlled Windmill

This paper aims at underlining the existence of some generic properties of windmilling flows, partially spread in the literature but never clearly stated. Two kinds of axial machines are investigated from compressor mode to highly loaded windmill: a conventional fan with poor turbine performance and an optimized fan able to reach high efficiencies in both compressor and windmilling operations. Both simulations and experiments are used to perform the analysis. Three particular behaviors were identified as typical of fans operating at windmill: the inverse stacking of the speed lines visible in (Π, Q_m) turbine maps, the appearance of a slope change on the loading-to-flow coefficient diagram at windmill, and a threshold effect occurring at highly loaded windmill.
[DOI: 10.1115/1.4040678]

Introduction

In a near future, with the concept of more electric aircraft, the need for onboard electrical energy will become a subject of great interest for manufacturers. From this perspective, several studies are currently carried out to investigate any potential energy source among existing onboard equipment. An axial fan (diameter < 200 mm), located downstream of an air intake in the underbelly of the aircraft, is part of them (Fig. 1). Its role is to cool heat exchangers when the airplane is on the ground. During the flight, the ram air is supplied with a high massflow by a NACA intake. The engine of the fan is turned off therefore the fan windmills freely under the incoming flow. The idea is to capitalize the equipment throughout the mission by turning the fan into a reversible turbomachine, working as a fan on the ground to cool heat exchangers and as a turbine in flight to recover electrical power.

In aeronautics, the windmilling phenomenon is described as the spontaneous rotation of a rotor under the effect of a moving fluid. This mode can be considered as a "functional" off-design operation of conventional fans, according to Binder [1]. It corresponds to situations when the sign of the work exchange is inverted compared with that of the design specification. Three regimes have been identified so far for windmilling situations: the locked rotor case (no rotation, high resistive torque) for which no energy is recoverable, freewindmill (high rotational speed, small resistive torque) for which a negligible energy is retrieved, and load-controlled windmill which corresponds to an intermediate regime between the previous

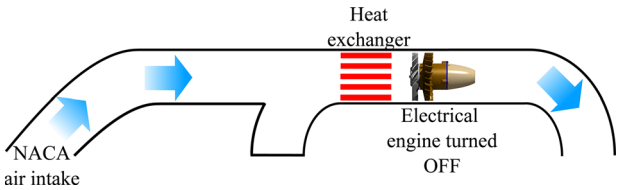

Fig. 1 Configuration in flight conditions

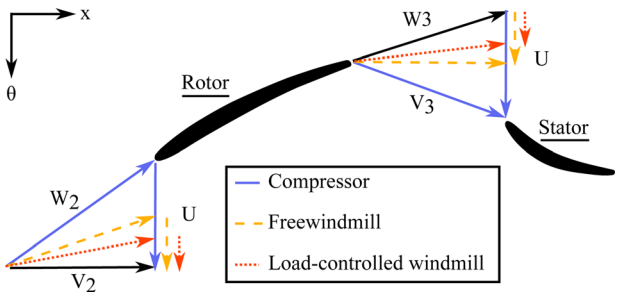

Fig. 2 Velocity diagrams in compressor mode, freewindmill, and load-controlled windmill for a conventional axial fan

[1]Corresponding author.

ones and which enables a significative energy recovery. Windmilling flows are generally associated with negative incidences and flow separations on the concave side of the blades. A simple way of understanding the basic mechanisms is to focus on the velocity diagram evolution from compressor mode to load-controlled windmill (Fig. 2). A purely axial incoming flow and a constant massflow at inlet are considered for simplicity's sake.

The literature generally focuses on the freewindmilling case to assess the relight capabilities and the drag contribution of multistage turbomachineries in engine-out conditions [2–6]. In this regime, the most surprising behavior reported so far is the radial antagonist functioning of the rotor blade: outboard profiles near the shroud are reported to work as a turbine whereas inboard ones near the hub operate as a compressor. This result was observed many times in the literature. Recent studies also demonstrated that this mixed behavior is also observed chordwise [7]: in the region near the leading edge, the blade operates as a turbine whereas the remaining surface works as a compressor.

Regarding load-controlled windmill, little information was available in the literature until the last 3 years, from which dedicated contributions began to appear [7–11]. From the time being, no work enabled to underline some unexpected behaviors typical of this severe far off-design regime; it is the objective of the present work. Here, three particularities of windmilling flows are pointed out: the inverse stacking of the speed lines compared with classical turbine maps, the appearance of a slope change on the loading-to-flow coefficient diagram at windmill, and a threshold effect occurring at highly loaded windmill. However, the existence of a slope change on the characteristic has already been witnessed in the literature near surge. McKenzie [12] explains that the loading-to-flow coefficient diagram corresponds to a straight line for which the slope depends on the rotor outlet relative angle. The author underlines that near surge this angle grows more quickly than the incidence (in other words, than the flow coefficient), leading to a deflection of the characteristic. The slope is thus reduced at the lowest flow coefficients. In the present work, a similar phenomenon is reported to occur at windmill but this time for negative incidences, as will be shown below.

To summarize, in this paper, three major topics are investigated on a conventional fan and on an optimized one in an attempt to identify the specific and generic windmilling properties:

- the inverse stacking of the speed lines visible in (Π, Q_m) turbine maps of axial fans operating in windmilling conditions;
- the existence of a slope change at windmill in the loading-to-flow coefficient diagram;
- the existence of a threshold at highly loaded windmill from which the flow properties do not evolve anymore in both rows.

Machines and Formalisms

All the machines investigated in this study are low-speed, low-dimension axial fans of rotor–stator type (diameter < 200 mm). The first one is a conventional fan, corresponding to the onboard original machine meant for the cooling of heat exchangers on the ground. It was classically designed as a fan for a given massflow and pressure ratio. The second fan is a dual machine, dedicated to both compressor and windmilling modes. Studies focused on the

Table 1 Geometric properties of axial machines

	Conventional fan	Dual machine
Diameter (mm)	$D < 200$	200
Number of rotor blades	$Z_R = 17$	13
Number of stator blades	$Z_S = 23$	27
Fan design speed (rpm)	$N \approx 12{,}000$	20,000
Fan design point	$\hat{\phi}^* = 0.66$	0.7
	$\hat{\psi} = 0.43$	0.30
Turbine design point	$\hat{\phi}^* = -$	1.5
	$\hat{\psi} = -$	–0.48

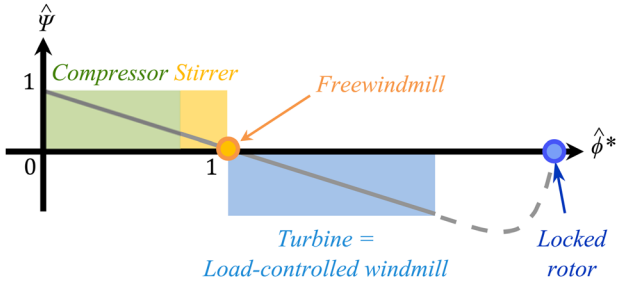

Fig. 3 Illustration of the functioning modes along the loading-to-reduced flow coefficient diagram

performance degradation of the conventional fan from compressor to highly loaded windmill and enabled to design the new machine, thanks to a nonconventional procedure [9,13]. For the optimized geometry, the original fan performance had to be reached while preserving the same diameter (limited by the size of the vein). The nonconventional design requires higher rotational speeds. The rotor was optimized in terms of blades angles and chord in order to be suitable for positive and negative work exchange and to suppress the mixed local behavior recorded at freewindmill. In addition, a variable camber stator was imagined to minimize the losses in both operations. During the experimental campaign, fixed removable stators with opposite camber were used. Some properties are given in Table 1 but confidentiality forbids a full description of the geometry.

Both machines were studied from compressor stall to highly loaded windmill. In this paper, two formalisms are used to represent their performance: the classical map involving the massflow and pressure ratio, and the $(\hat{\psi}, \hat{\phi}^*)$ characteristic which is a loading-to-reduced flow coefficient diagram (Eqs. (1)–(3)). This last representation slightly differs from the literature definition, mainly regarding the reference radius chosen (Eqs. (4) and (5)). Moreover, a reduction of the flow coefficient $\hat{\phi}$ by its value at freewindmill $\hat{\phi}_P$ is used ($\hat{\phi} = \hat{\phi}_P$ when $\hat{\psi} = 0$). It enables to clearly identify compressor ($\hat{\phi}^* < 1$) and turbine ($\hat{\phi}^* > 1$) operating ranges and allow a more direct comparison of different geometries: simplified theoretical development shows that any geometry should produce a unique operating line in that map, passing through (0, 1) and (1, 0)

$$\hat{\psi} = \frac{\Delta h_{i23}}{\hat{U}^2} \tag{1}$$

$$\hat{\phi} = \frac{V_{x2}}{\hat{U}} \tag{2}$$

$$\hat{\phi}^* = \frac{\hat{\phi}}{\hat{\phi}_P} \tag{3}$$

$$\hat{r} = \sqrt{\frac{r_{\text{shroud}}^2 + r_{\text{hub}}^2}{2}} \tag{4}$$

$$\hat{U} = \omega \hat{r} \tag{5}$$

This $(\hat{\psi}, \hat{\phi}^*)$ formalism is particularly suitable for dual functioning because the compressor operation, the stirrer mode (compressor operation for which the work input does not compensate for the losses), and all possible windmilling regimes can be represented on this unique line, regardless of the considered machine (Fig. 3).

Experimental Setup

The experimental study is carried out in the Department of Aerodynamics, Energetics and Propulsion (DAEP) of ISAE-SUPAERO. A test facility, named WILLOW for WIndmilL LOW-Reynolds, dedicated to the windmilling of low-dimension axial fans (diameter < 200 mm) has been developed and is

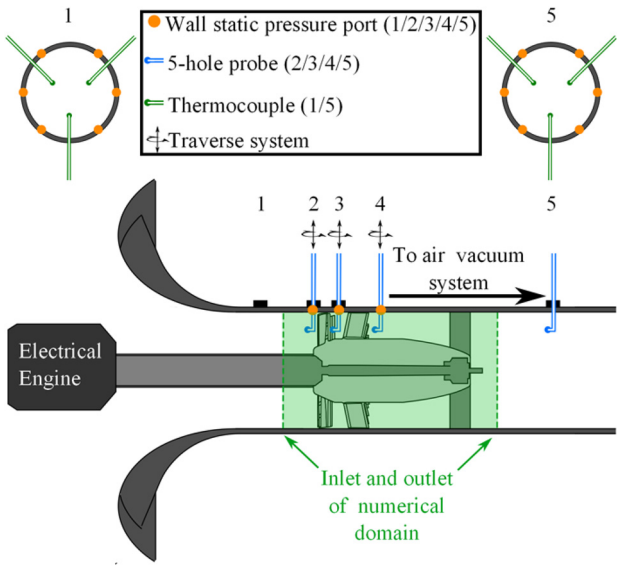

Fig. 4 Illustration of the DAEP windmilling test facility of ISAE-SUPAERO (WILLOW)

illustrated in Fig. 4 together with the associated instrumentation. A dual management of the energy (air vacuum system and asynchronous electrical engine) allows the independent setting of flow generation by suction and shaft loading. The latter and the rotational speed are measured and controlled by the differential transformer torque meter (Magtrol TM 306) coupled with the electrical engine. Thanks to this regulation system, a complete exploration of the operating line is possible: from surge limit to locked rotor configuration. In addition, the test section is reversible to invert the flow direction, if required. This means that the whole test rig configuration is designed to enable a complete four-quadrant characterization of the axial fans, as presented in Ref. [14]. The maximum rotational speed reachable experimentally is 18,000 rpm but due to critical vibrations of the bench, the results presented in this paper were obtained for a limited value of 10,000 rpm. An electronic rack composed of resistances is provided to absorb the generated energy in windmilling operation. The air vacuum system is equipped with five liquid-ring pumps. Each of them can generate a maximum massflow of 1 $m^3 s^{-1}$.

Table 2 95% confidence intervals for global measurements in compressor mode, freewindmill, and load-controlled windmill [Experimental]

$\hat{\phi}^*$	$\hat{\psi}$	Π	η
0.656 ± 0.005	0.367 ± 0.008	1.016 ± 0.003	0.80 ± 0.01
1.001 ± 0.005	–0.020 ± 0.013	0.982 ± 0.005	—
2.000 ± 0.006	–1.396 ± 0.036	0.961 ± 0.003	0.16 ± 0.01

Both global and local measurements are implemented to quantify the power recovery and to study the flow topology around the rotor and around the stator. A detailed description of the instrumentation regarding the planes 1, 2, 3, and 5 is available in Refs. [13] and [15]. In the present paper, a third-directional five-hole probe is used (Plane 4) around 27.5 mm downstream the trailing edge of the stator (Keller, –150/+100 mbars, basic accuracy 0.047% FS, Rosemount –50/50 mbars, basic accuracy 0.15% FS).

All pressure sensors (Rosemount, Keller) used for the measurements were the objects of an in-house calibration beforehand. In addition, as the instrumented section is generally subjected to dust and pollution, the five-hole probes were regularly cleaned with alcohol in order to avoid the damage in the accuracy of the steady-state measurements. A procedure dedicated to the setup of the five-hole probes angular reference was also developed. The absolute uncertainty of raw variables was calculated based on that of the sensors. For the calculated parameters, the absolute uncertainty was assessed by the composition of the relative uncertainty of each raw variables involved in its expression.

For the conventional fan, a repeatability study was carried out on the global and local measurements. The student's *t*-distribution was applied over a sequence of several tests for a 95% confidence interval. Three operating points were investigated: in compressor mode, in freewheeling condition, and at load-controlled windmill. The

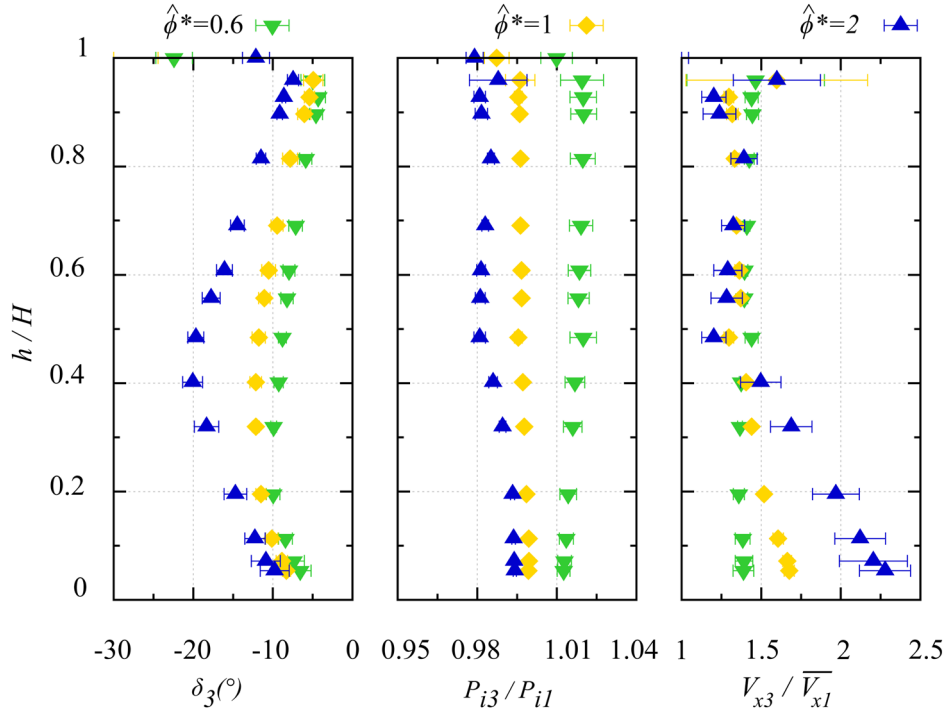

Fig. 5 95% confidence intervals for five-hole probe measurements at rotor outlet in compressor mode, freewindmill, and load-controlled windmill [experimental]

results are visible in Table 2 for the global measurements. The scattering on the performances is rather small and appears independent of the operating point, except for the loading coefficient.

The repeatability of the local measurements coming from the five-hole probe at rotor outlet is presented in Fig. 5. An acceptable scattering is recorded for the three parameters, especially at free-windmill. On the whole, for all the measurements, the repeatability error was found to be greater than the measurement uncertainties and shall be considered instead. It is not indicated in the results of this paper for clarity reasons. Generally, it remains in the range of the symbol size.

Numerical Setup

For the purposes of the study, numerical simulations were performed to bring additional information to the experimental data in order to complete the analysis.

The calculations were carried out, thanks to the Euranus solver of FINE^{TM}/Turbo V9.0.2, a commercial CFD suite developed by Numeca. This is a three-dimensional, density-based code that is dedicated to the study of flows in turbomachines. For the computations, the steady mixing-plane approach was chosen. Local-time stepping is used. The advance in pseudo-time is ensured by a four-stage Runge–Kutta scheme. The relevance of turbulence closure models regarding windmilling flows predictivity was investigated in a previous work [16]. According to the latter, two models stand out and are equivalent: the two-equation SST model [17] and the one-equation Spalart–Allmaras model [18,19]. In this study, the first one was chosen for all calculations. One motive led to this choice: academically, the literature seems to recommend the SST model for light or deep stall cases because the Spalart–Allmaras model usually underpredicts the separation [20–22]. The turbulence intensity was calculated based on the Reynolds number and is about 3%. It is used to calculate the turbulent kinetic energy k using a reference velocity determined from the massflow. A turbulent dissipation rate ε is also calculated from a turbulence length scale. Both k and ε are imposed uniform at the inlet section only. A fully turbulent flow is assumed. Uniform absolute total pressure and temperature are imposed at inlet. At outlet, the massflow is imposed with pressure adaptation. Convective fluxes are determined by a second-order centered scheme with added Jameson artificial dissipation [23].

The numerical domain is illustrated in Fig. 4. As visible, the shaft, the bell mouth, and the rear support, present on the experimental facility, are not numerically represented. The domain is discretized with a multiblock-structured mesh generated with AutoGrid 5^{TM}, a module of FINE/Turbo. The mesh, illustrated in Fig. 6 for the conventional fan, consists of O-grid blocks located around the blades and H-grid blocks in the passage. A mesh of 5M points was used for this study (rotor: 2.2 M, stator: 1.8 M). The number of flow paths is 121 in the rotor (including 33 points in the tip gap) and 89 in the stator. The number of cells in the pitchwise direction is 51 in the rotor and 59 in the stator. The convex and concave blade surfaces are discretized with 117 grid points in the rotor and 97 in the stator. The first cell at wall was set to 3 μm. The mesh quality parameters are given in Table 3.

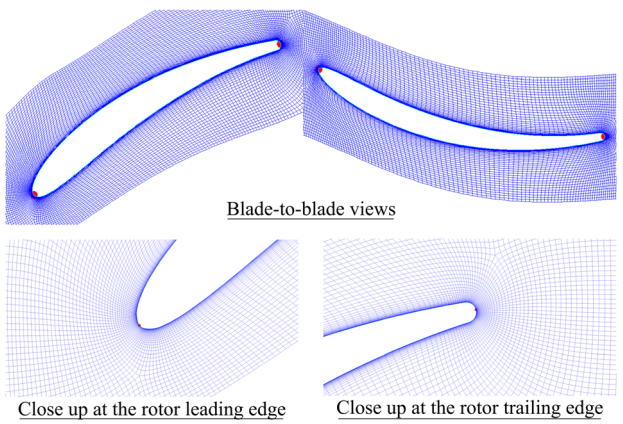

Fig. 6 Mesh visualizations

Table 3 Quality parameters of the 5M points mesh for the steady mixing-plane calculations

	Min skewness	Max aspect ratio	Max expansion ratio	y^+_{mean}	y^+_{max}
Rotor	32	430	2.33	0.28	1.54
Stator	36	216	1.79	0.31	1.42

A mesh sensitivity study was performed on the conventional fan for the most loaded operating point studied at windmill, namely $\hat{\phi}^* = 3$. Four meshes were tested with a total size of about 1.5, 5, 8, and 10 M points. Regarding the global performance, no clear improvement was witnessed, despite small changes in loading coefficient. In any case, the variations related to the mesh dependency were smaller than the experimental uncertainties previously presented. From a local point of view, the radial distributions around the rotor and the stator were examined. The mesh convergence was not fully reached even with a 10 M points mesh, but a reasonable compromise seemed to be the 5 M points mesh, since the coarsest one was not able to properly capture the physics of the flow especially at stator inlet. More details about this study are available in Ref. [13].

Inverse Stacking of Speed Lines on Turbine Maps

This section deals with a particularity of the turbine maps obtained for fans operating at windmill. An insight into these experimental classical representations is given in Fig. 7 for the conventional fan on the left and the dual machine on the right. Five rotational speeds and different valves conditions were investigated at windmill for both machines.

One noticeable result is the inverse stacking of the speed lines. Contrary to conventional axial turbine maps [24], for a given massflow, increasing the rotational speed leads to a decrease in pressure ratio for both fans operating in windmilling conditions. This can be explained by the theoretical evolution of the rotor total enthalpy variation with the blade speed U for a fixed axial velocity. The corresponding equation, given by Courty-Audren in Ref. [9], is derived from the analytical $(\hat{\psi}, \hat{\phi})$ model [8] and expressed in the following equations:

$$\Delta h_i = \hat{U}\left(\hat{U} + \hat{n} V_{x2}\right) \tag{6}$$

$$\hat{n} = \frac{V_{x3}}{V_{x2}} \tan \hat{\beta}_3 - \tan \hat{\alpha}_2 \tag{7}$$

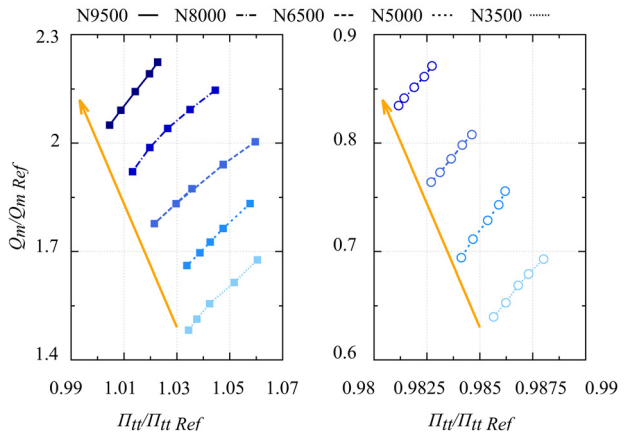

Fig. 7 Classical turbine maps for the conventional fan (left) and the dual machine (right) [experimental]

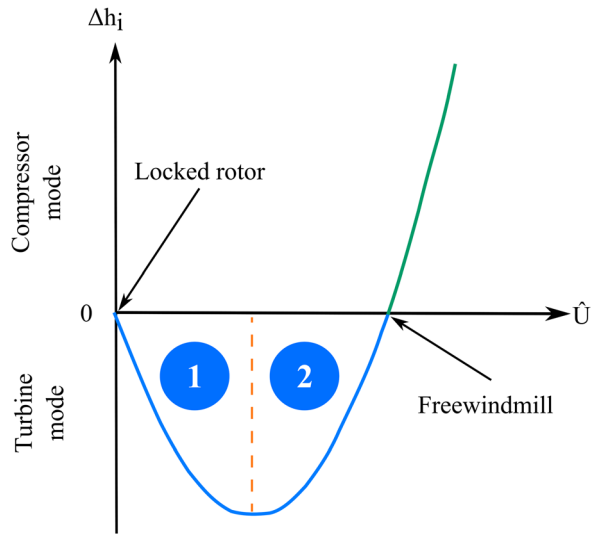

Fig. 8 Evolution of the total enthalpy variation with the blade speed for a given axial velocity, from Ref. [9] [analytical]

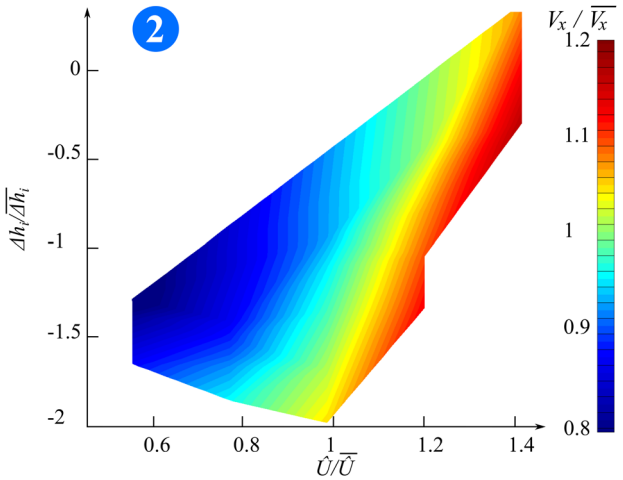

Fig. 9 Evolution of the total enthalpy variation with the blade speed for a given axial velocity, for the conventional fan [experimental]

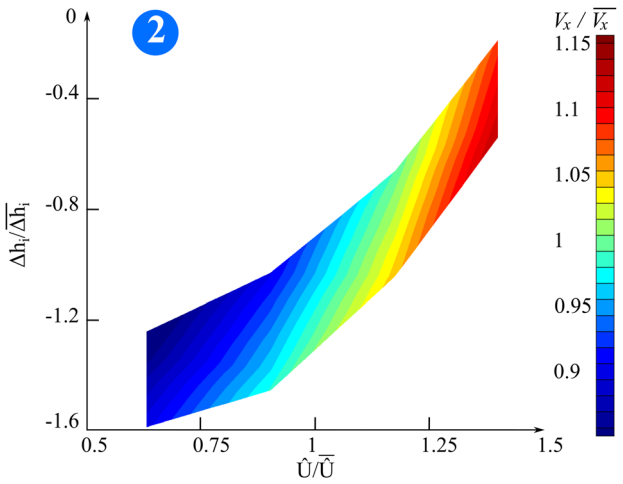

Fig. 10 Evolution of the total enthalpy variation with the blade speed for a given axial velocity, for the dual machine [experimental]

The curve corresponding to Eq. (6) is presented in Fig. 8. It shows how the work evolves with the blade speed, for a given axial velocity, in compressor and turbine operations for a conventional fan. A minimum exists for the negative values of total enthalpy variation and corresponds to a blade speed and a reduced flow coefficient is defined as follows:

$$\hat{U}_{\text{Min}} = -\frac{\hat{n}V_{x1}}{2} \tag{8}$$

$$\hat{\phi}^{*}_{\Delta h_{i\text{Min}}} = -\frac{2}{\hat{n}\hat{\phi}_P} \tag{9}$$

The minimum in enthalpy variation obtained for the turbine operation underlines the existence of two zones for which the increase in blade speed leads to either an increase or a decrease in work (respectively, zones 1 and 2). The experimental curves corresponding to the previous turbine maps (Fig. 7) are given in Figs. 9 and 10 for the conventional fan and the dual machine, respectively. As visible on the two contours, the operating points are all included in zone 2 where the work and the blade speed have an opposite variation direction. This is not surprising since dual fans shall work in both compressor and turbine operations which means that they necessarily operate near the freewheeling point.

For the purpose of the analysis, conventional turbines are now considered. In this case, the presence of the stator in front of the rotor is responsible for a great positive value of α_2 in Eq. (7). This entails a more negative value of $\hat{n}$ which leads to a displacement of the work minimum toward higher rotational speeds, according to Eq. (8). Consequently, conventional loaded turbines are expected to work in zone 1. According to this explanation, less loaded turbines or conventional fans, characterized by small values of α_2, are believed to work in zone 2, with a work minimum located toward the lowest rotational speeds.

An analytical method developed by Lagha [25] in order to switch from (Π, Q_m, η, N) to (ψ, ϕ, η) maps is used to check the previous explanation. Starting from the $(\hat{\psi}, \hat{\phi}^{*})$ characteristic and for a given rotational speed, this tool also predicts the inverse stacking observed at windmill for the present axial fan. In addition, Lagha's methodology allows to extract the work evolution with the blade speed from a (Π, Q_m, η, N) map. This has been applied on conventional axial turbine maps, available from Proosis gas turbine simulation software [26], for which a classical stacking is observed. As could have been expected, they were reported to be located in zone 1 (Fig. 11). This result confirms that the stacking of the speed lines is directly related to the variation of the work evolution with the blade speed.

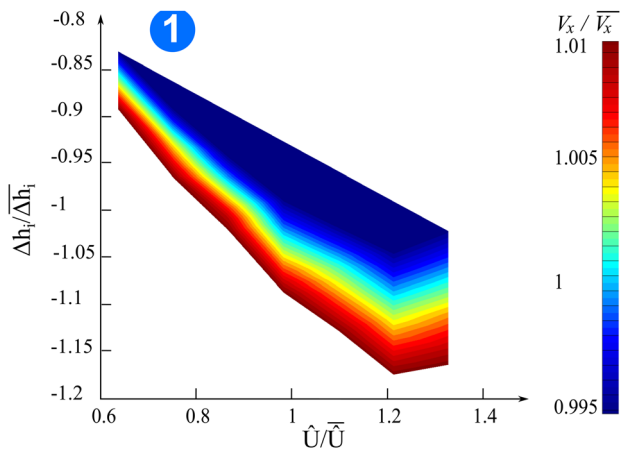

Fig. 11 Evolution of the total enthalpy variation with the blade speed for a given axial velocity, for a generic axial turbine map from Proosis [numerical]

Threshold Effect at Highly Loaded Windmill

The local flow properties at rotor and stator outlets were investigated along the operating line for nine points: three in compressor mode ($\hat{\phi}^* = 0.6$, $\hat{\phi}^* = 0.66$, $\hat{\phi}^* = 0.8$), freewindmill ($\hat{\phi}^* = 1$) and five at load-controlled windmill ($\hat{\phi}^* = 1.2$, $\hat{\phi}^* = 1.5$, $\hat{\phi}^* = 2$, $\hat{\phi}^* = 2.5$, $\hat{\phi}^* = 3$). The identification of the phenomenon described below was possible because experiments were carried out at highly loaded windmilling operation. Figures 12–14 present the evolution of the radial distribution of work and losses with the reduced flow coefficient for the conventional fan (left figure) and the dual machine (right figure).

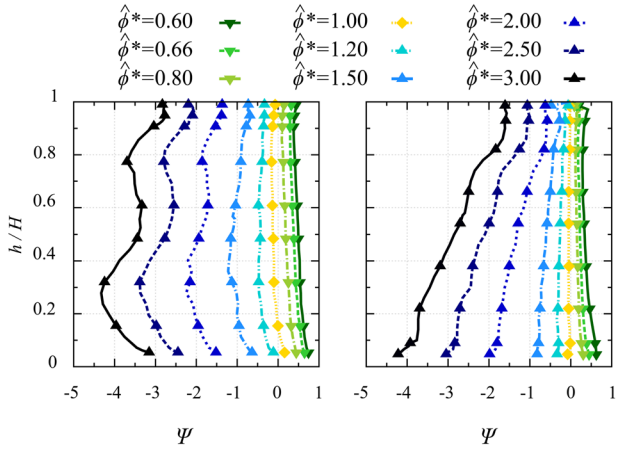

Fig. 12 Rotor work evolution for the conventional fan (left) and the dual machine (right) [experimental]

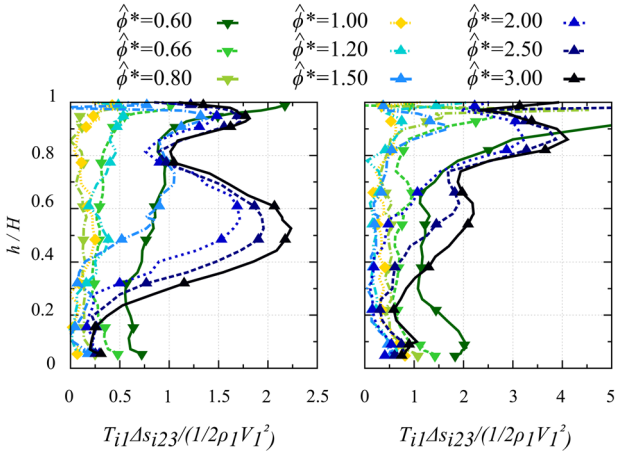

Fig. 13 Rotor losses evolution for the conventional fan (left) and the dual machine (right) [experimental]

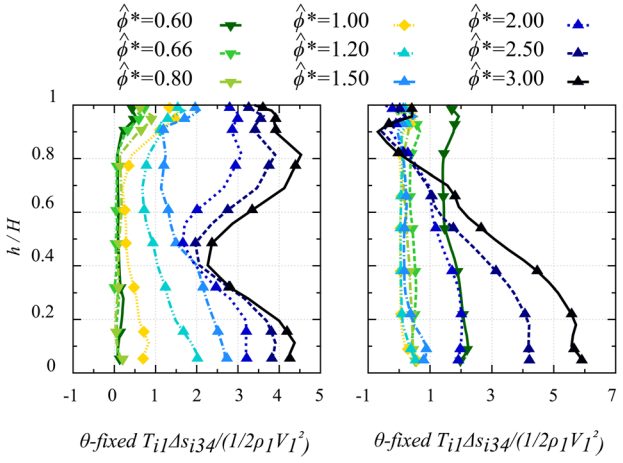

Fig. 14 Stator losses evolution for the conventional fan (left) and the dual machine (right) [experimental]

For both machines, the flow local topology seems to evolve continuously from compressor to moderated load-controlled windmill. However, above a critical value ($\hat{\phi}^* = 1.5$ for the conventional fan and $\hat{\phi}^* = 2$ for the dual machine), the flow properties appear significantly different, underlining a clear radial distortion for the highly loaded windmilling cases. This strong change of topology was recorded for all the flow variables but is particularly visible on the losses and on the rotor outlet deviation (not presented here). For the highest values of reduced flow coefficient, the topology does not seem to evolve anymore in both rows. In a near future, a locked rotor experiment will be carried out on both machines in order to confirm this point. The threshold effect seems correlated to the nonevolution of the stator separation when it reaches the last remaining sections of the blades (not separated yet). Then, the expansion of the separation is only possible in the azimuthal direction which is also limited by the presence of the mainflow. This effect has been witnessed for both machines. This may suggest that the threshold effect is linked to the stator separation topology, at least for the fans of this study. Indeed, both stators are characterized by blades that are more cambered and more numerous than the rotor ones which means that the most negative incidences and the smallest passages are found in the stator where massive separations are first observed.

Slope Change at Windmill

Figures 15 and 16 show the $(\hat{\psi}, \hat{\phi}^*)$ characteristic of the conventional fan and the dual machine, respectively. The performance with symbols has been obtained experimentally from compressor stall to highly loaded windmill with a discretization of $\Delta\hat{\phi}^* = 0.05$. Linear fits have been added to emphasize the existence of linear evolutions and thus underline that a slope change occurs for both machines. In addition, the numerical performance obtained with mixing-plane simulations has been added in solid lines for both machines and also shows a slope change. The reduced flow coefficient, $\hat{\phi}^*_{sc}$, corresponding to this phenomenon is indicated in the figures and is reported to be very different for both machines, but located in the windmilling operating range.

Since this slope change is visible on the loading coefficient evolution, it shall be related to the work exchange and therefore to the rotor topology. This phenomenon is also visible on the

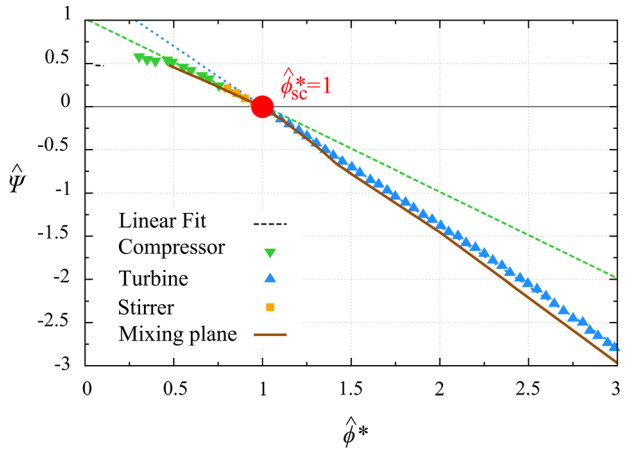

Fig. 15 Loading-to-reduced flow coefficient diagram for the conventional fan

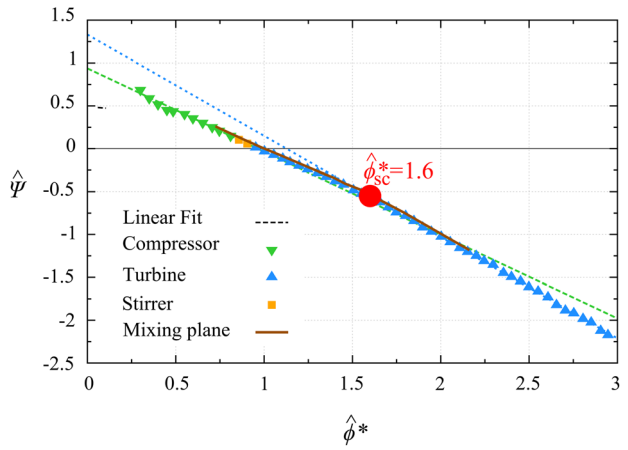

Fig. 16 Loading-to-reduced flow coefficient diagram for the dual machine

simulations for both machines (results not presented here). Consequently, its origin was numerically investigated by focusing on the flow inside the rotor near the $\hat{\phi}^*_{sc}$ point. Actually, the slope change seemed to be related to the appearance of a tornado-like vortex shortly after the beginning of the rotor separation. The results are given for the conventional fan in Fig. 17 and for the dual machine in Fig. 18. The two-dimensional shape of the separation is underlined by the viscous stress lines plotted on the blade skin whereas its three-dimensional topology is presented by means of streamlines colored with the reduced radial velocities. After the reduced flow coefficient for which the slope change is recorded, a tornado-like vortex begins to appear for both machines, along with the displacement of the reattachment line toward the trailing edge. This vortex inside the separated area impacts the blade loading and therefore the work and deviation. For a purely axial incoming flow, the deviation is directly involved in the slope of the $(\hat{\psi}, \hat{\phi}^*)$ characteristic, together with the rotor outlet axial velocity ratio (Eq. (7)). Consequently, the deviation is believed to increase more quickly than the incidence (in other words than the flow coefficient), leading to a more steeper slope.

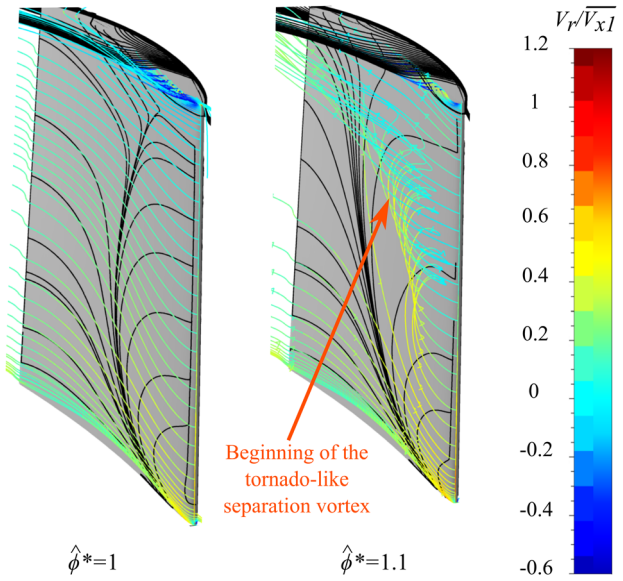

Fig. 17 Beginning of the rotor separation topology near the slope change point for the conventional fan: viscous stress lines plotted on the blade skin with streamlines colored by the absolute radial velocity [steady-state mixing-plane simulation]

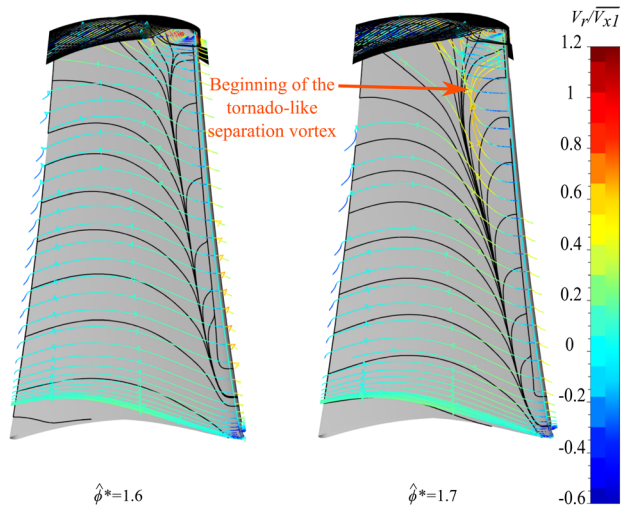

Fig. 18 Beginning of the rotor separation topology near the slope change point for the dual machine: viscous stress lines plotted on the blade skin with streamlines colored by the absolute radial velocity [steady-state mixing-plane simulation]

The "windmilling slope change" could be to negative incidences where the "surge slope change," pointed out by McKenzie [12], is to positive incidences, the separation occurs this time on the concave side of the blades instead of the convex side. The flow coefficient corresponding to the slope change differs from one fan geometry to another and is hard to predict since it depends on several parameters: the amount of negative incidence, the leading edge shape, the blade camber, the solidity, and the radial stacking. Further investigation is needed, in particular on other fans' geometries, in order to confirm the generic property of the slope change. Taking into account, this phenomenon can be particularly important for low-order methods that aim at predicting the windmilling performance. Generally, analytical models remain predictive only up to the slope change. This point is tackled in Analytical Prediction of Windmilling Performance.

Analytical Prediction of Windmilling Performance

Low-order methods are really adapted to preliminary design issues. The $(\hat{\psi}, \hat{\phi}^*)$ approach seems to be a promising base for a multiquadrant design tool, provided that the windmilling performance is well assessed. Here, the predictivity of the global formulation of the analytical $(\hat{\psi}, \hat{\phi}^*)$ model, presented in detail by Binder

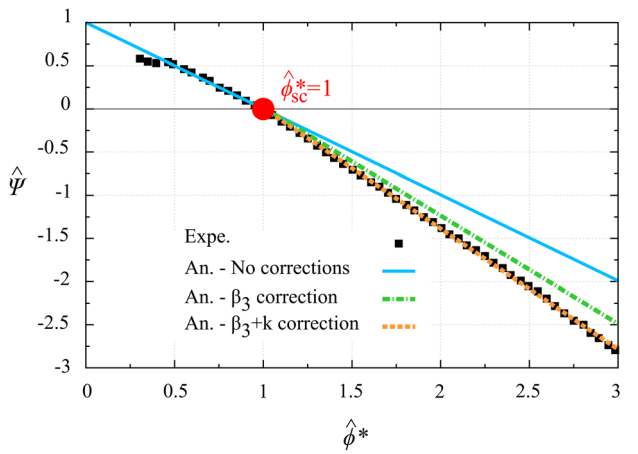

Fig. 19 Loading-to-reduced flow coefficient diagram for the conventional fan [experimental/analytical]

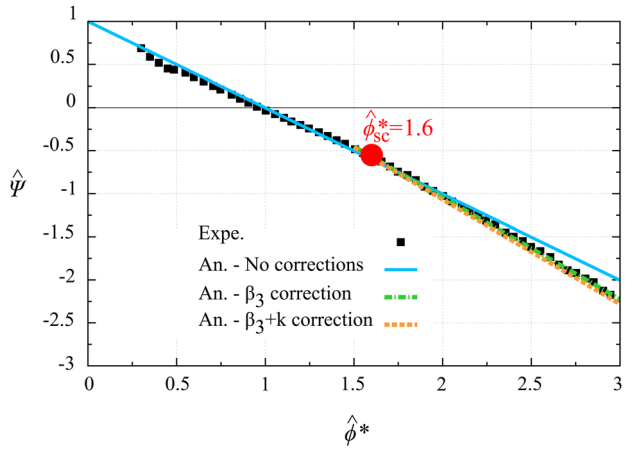

Fig. 20 Loading-to-reduced flow coefficient diagram for the dual machine [experimental/analytical]

Table 4 Modifications of $(\hat{\psi}, \hat{\phi}^*)$ model coefficients

	$\hat{\phi}^* \leq \hat{\phi}^*_{sc}$	$\hat{\phi}^* \geq \hat{\phi}^*_{sc}$
V_{x3}/V_{x2}	A_2/A_3	$1.1 \times A_2/A_3$
β_3	$\beta_3' + \delta_{Carter}$	$\beta_3' + \delta_{Carter} - 7$ deg

and Courty-Audren in Refs. [8] and [9], is assessed from experimental data for the conventional fan and the dual machine.

The global performance predicted by the analytical model is presented in blue solid line in Figs. 19 and 20 for both machines. For information purposes, in this model, the deviation angle needed to calculate the slope of the characteristic is modeled using Carter's rule, as recommended by Prasad and Lord [6]. Compared with experimental data, for both machines, the model well captures the performance until the slope change is reached. From this point, a discrepancy arises and increases with the flow coefficient. Since the actual outlet flow angle is characterized by a highly radially distorted distribution [15], the prediction of the deviation is no longer accurate.

In the mean line approach, the theoretical analysis (Eq. (7)) suggests two possible origins for the bad prediction of the performance at windmill: the relative flow angle at rotor outlet and the rotor axial velocity ratio. It is interesting to determine the extent to which each parameter plays a role in the actual slope change. This will underline the points on which the improvement of the analytical model should focus on future work. Corrections of the model have been performed using windmilling test data. These corrections consist of an empirical resetting for a better understanding of the phenomenon.

Several corrective attempts were performed to match the experimental performance. Finally, the adopted methodology consisted in considering the tests data of β_3 and V_{x3}/V_{x2} after the occurrence of the threshold. This led to the same amount of corrections of these parameters for both machines, despite clear differences in the rotor geometries. These corrections are indicated in Table 4 and plotted in green and orange lines in Figs. 19 and 20. They are implemented from $\hat{\phi}^*_{sc}$ for clarity reasons. As visible, the deviation is responsible for most of the slope change. This strengthens the necessity of developing deviation rules specific to load-controlled windmill to well predict the performance, as already stated in Ref. [15]. These corrections were established in an empirical way, and cannot be generalized without further analysis upon a large number of different machines. As the deviation seems to play a major role, the solidity and stagger angle may be the most relevant parameters for a proper generalization of these corrections. The reason why the rotor axial velocity ratio has a stronger impact on the conventional fan lies in the presence of a vein contraction in the conventional rotor (stemming from a change in hub radius at a constant shroud radius) contrary to the optimized fan.

Conclusion

The objective of this paper was to present three particular phenomena, not identified so far, that are expected to be generic for conventional fans operating at windmill. In the literature, studies do not investigate windmilling flows in such a far off-design range. This explains why the discovered phenomena are relatively new. Main findings can be summarized as follows:

- an inverse stacking of the speed lines in turbine maps was recorded in this study and is believed to be generic for fans operating at windmill and for lowly loaded turbines in a more general way. The corresponding explanation lies in the evolution of the work exchange with the blade speed. Moreover, this result can be very useful regarding maps extrapolations;
- a strong change of topology was observed on the radial distributions at highly loaded windmill leading to a threshold effect from which the flow properties does not evolve anymore in both rows. This phenomenon is likely to be triggered when the separation becomes massive, which first occurs in the stator for the machines of this study. More specifically, it seems to happen when the separation radially reaches the last blades profiles and mostly expands in the pitchwise direction;
- the existence of a slope change in the $(\hat{\psi}, \hat{\phi}^*)$ characteristic occurring in the windmilling range was reported. This phenomenon can be imputed to the appearance of a tornado-like vortex in the rotor separated area. It mainly results in an increase in the rotor outlet deviation. This slope change can be analytically modeled by taking into account a modification of the deviation and rotor outlet axial velocity ratio. It leads to a good agreement with tests data. This means that the $(\hat{\psi}, \hat{\phi}^*)$ approach can be used for the assessment of multiquadrant machines performance since a single modification of the model coefficients is needed to represent the complete operating line. The "windmilling slope change" is believed to be to negative incidences where the "surge slope change" is to positive incidences.

Acknowledgment

The present work is performed within the scope of the CORAC GENOME project, which aims at optimizing the power management and finding new energy sources in more electric aircraft [27]. The CORAC consortium was created in 2008 on the French government initiative to harmonize the research efforts in aeronautics related to environment preservation and sustainable development. The authors would also like to express their gratitude to the technical staff who did a remarkable work regarding the numerous dismantling/assemblies of the facility as well as the implementation of the instrumentation. Without their assistance, the results presented in this paper would have never been established.

Nomenclature

Roman symbols

A = area (m^2)
h_i = absolute total enthalpy (J kg^{-1})
P_i = absolute total pressure (Pa)
Q_m = massflow (kg s^{-1})
r = radius (m)
U = blade speed (m s^{-1})
V = absolute velocity (m s^{-1})

V_r = radial absolute velocity (m s^{-1})
V_t = tangential absolute velocity (m s^{-1})
V_x = axial absolute velocity (m s^{-1})
W = relative velocity (m s^{-1})

Greek Symbols

α = absolute flow angle (deg)
β = relative flow angle (deg)
δ = rotor outlet deviation (deg)
η = isentropic efficiency
Π = pressure ratio
ρ = density (kg m^{-3})
ϕ = flow coefficient
ϕ_P = flow coefficient for the freewheeling operating point
$\hat{\phi}^*$ = reduced flow coefficient
ψ = loading coefficient
ω = angular blade speed (rad s^{-1})

Subscripts

1 = inlet
2 = rotor inlet
3 = rotor outlet
4 = stator outlet
5 = outlet
tt = total-to-total variable

Superscript

$\hat{}$ = assessed at the rotor outlet mean quadratic radius

Acronyms and Abbreviations

FS = full scale
NI = national instrument

References

[1] Binder, N., 2016, "Aérothermodynamique Des Turbomachines En Fonctionnement Hors-Adaptation," Habilitation thesis, ISAE-SUPAERO, Toulouse, France.
[2] Dufour, G., Margalida, G., and García Rosa, N., 2015, "Integrated Flow Simulation of the Fan and High-Pressure Compressor Stages of a Turbofan at Windmill," Tenth European Conference on Turbomachinery, Madrid, Spain, Mar. 23–27, Paper No. ETC2015-150.
[3] Garcia Rosa, N., Pilet, J., Lecordix, J.-L., Barènes, R., and Lavergne, G., 2013, "Experimental Analysis of the Flow Through the Fan Stage of a High-Bypass Turbofan in Windmilling Conditions," Tenth European Conference on Turbomachinery, Lappeenranta, Finland, Apr. 15–19, Paper No. ETC2013-162.
[4] Gunn, E. J., and Hall, C. A., 2016, "Loss and Deviation in Windmilling Fans," ASME J. Turbomach., **138**(10), p. 101002.
[5] Mohankumar, B., and Wilson, M. J., 2017, "Rotational Speed of a Damaged Fan Operating at Windmill," 12th European Conference on Turbomachinery, Stockholm, Sweden, Apr. 3–7, Paper No. ETC2017-096.
[6] Prasad, D., and Lord, W. K., 2010, "Internal Losses and Flow Behavior of a Turbofan Stage at Windmill," ASME J. Turbomach., **132**(3), p. 031007.
[7] Hirayama, T., Ohta, Y., Goto, T., and Kato, D., 2017, "Internal Flow Structure and Rotor Performance of an Axial Flow Compressor at Windmill Conditions," 13th International Symposium on Experimental and Computational Aerothermodynamics of Internal Flows, Okinawa, Japan, May 7–11, Paper No. ISAIF13-S-0031.
[8] Binder, N., Courty-Audren, S.-K., Duplaa, S., Dufour, G., and Carbonneau, X., 2015, "Theoretical Analysis of the Aerodynamics of Low-Speed Fans in Free and Load-Controlled Windmilling Operation," ASME J. Turbomach., **137**(10), p. 101001.
[9] Courty-Audren, S.-K., 2015, "Identification Et Compréhension Des Mécanismes Aérodynamiques Liés Au Potentiel De Récupération D'énergie. Application à Un Ventilateur Axial Subsonique En Autorotation," Ph.D. thesis, ISAE-SUPAERO, Toulouse, France.
[10] Courty-Audren, S.-K., Carbonneau, X., Binder, N., and Challas, F., 2013, "Comparaison Des Méthodes Numériques Stationnaire Et Instationaires Dans La Prédiction D'écoulements Décollés," Congrès Français De Mécanique, Bordeaux, France, Aug. 26–30, pp. 1–6.
[11] Goto, T., Kato, D., Ohta, Y., and Outa, E., 2014, "Unsteady Flow Structure in an Axial Compressor at Windmill Condition," ASME Paper No. GT2014-25609.
[12] McKenzie, A. B., 1997, Axial Flow Fans Compressor—Aerodynamic Design Performance, Cranfield Series Turbomachinery Technology, Gower Technical, London, UK.
[13] Ortolan, A., 2017, "Aerodynamic Study of Reversible Axial Fans With High Compressor/Turbine Dual Performance," Ph.D. thesis, ISAE-SUPAERO, Toulouse, France.
[14] Turner, R. C., and Sparkes, D. W., 1963, "Complete Characteristics for a Single Stage Axial Flow Fan," Inst. Mech. Eng., **178**(9), pp. 14–27.
[15] Ortolan, A., Courty-Audren, S.-K., Carbonneau, X., Binder, N., and Challas, F., 2017, "Experimental and Numerical Flow Analysis of Low-Speed Fans at Highly Loaded Windmilling Conditions," ASME J. Turbomach., **139**(7), p. 071009.
[16] Thollet, W., 2013, "Numeca v9: Windmilling, Tech. Report, SAFRAN Ventilation Systems—Note technique Confidentielle," Report No. R&D-NT-135-2013.
[17] Menter, F. R., 1994, "Two-Equation Eddy-Viscosity Turbulence Models for Engineering Applications," AIAA J., **32**(8), pp. 1598–1605.
[18] Ashford, G. A., and Powell, K. G., 1996, "An Unstructured Grid Generation and Adaptative Solution Technique for High-Reynolds Number Compressible Flow," Ph.D Thesis, p. 230.
[19] Spalart, P. R., and Allmaras, S. R., 1992, "A One Equation Turbulence Model for Aerodynamic Flows," AIAA Paper No. AIAA-92-0439.
[20] Ekaterinaris, J. A., and Menter, F. R., 1994, "Computation of Oscillating Airfoil Flows With One- and Two-Equation Turbulence Models," AIAA J., **32**(12), pp. 2359–2365.
[21] Shur, M., Strelets, M., Zaikov, L., Gulyaev, A., Kozlov, V., and Secundov, A., 1995, "Comparative Numerical Testing of One- and Two-Equation Turbulence Models for Flows With Separation and Reattachment," AIAA Paper No. 95-0863.
[22] Spall, R. E., Phillips, W. F., and N, A., 2004, "An Assessment of Five Turbulence Models in Predicting Turbulent Separation," ASME Paper No. HT-FED04-56813.
[23] Jameson, A., 1991, "Time Dependent Calculations Using Multigrid, With Applications to Unsteady Flows past Airfoils and Wings," AIAA Paper No. 91-1596.
[24] Lakshminarayana, B., 1996, *Fluid Dynamics and Heat Transfer of Turbomachinery*, Wiley, Hoboken, NJ.
[25] Lagha, M., Duplaa, S., Binder, N., and Carbonneau, X., 2017, "Unified Classification and Characterization of Axial Turbomachines and Propellers," 13th International Symposium on Experimental and Computational Aerothermodynamics of Internal Flows, Okinawa, Japan, May 7–11, Paper No. ISAIF13-S-0038.
[26] Tsoutsanis, E., Meskin, N., Benammar, M., and Khorasani, K., 2015, "Transient Gas Turbine Performance Diagnostics Through Nonlinear Adaptation of Compressor and Turbine Maps," ASME J. Eng. Gas Turbines Power, **137**(9), p. 091201.
[27] Rosero, J. A., Ortega, J. A., Aldabas, E., and Romeral, L., 2007, "Moving Towards a More Electric Aircraft," Aerosp. Electron. Syst. Mag., **22**(3), pp. 3–9.